**SPECTRUM OF ENGINEERING SCIENCES**
ISSN (E) 3007-3138 (P) 3007-312X
**VOLUME 4, ISSUE 6, 2026**

# ECO-FRIENDLY FABRICATION OF MANGANESE–NICKEL–VANADIUM SULFIDE-BASED COMPOSITES WITH ZNO, $TIO_2$, AND AG FOR ENHANCED SUPERCAPACITOR PERFORMANCE

**Nida Afzal[*1], Syed Sajjad Hussain[2], Rida Tariq[3]**

*[*1]Department of Physics, University of Agriculture, Faisalabad, Punjab, Pakistan*
*[2]Department of Physics, University of Agriculture, Faisalabad, Punjab, Pakistan*
*[3]Department of Chemistry, COMSATS University Islamabad, Pakistan*

[*1]nidaafzal438@gmail.com, [2]syedsajjadh138@gmail.com, [3]tariqrida124@gmail.com

**DOI:** https://doi.org/10.5281/zenodo.20741229

**Keywords**
*supercapacitor; manganese–nickel–vanadium sulfide; ZnO; $TiO_2$; silver nanoparticles; green synthesis; hydrothermal; pseudocapacitance; energy storage*

**Article History**
*Received: 18 April 2026*
*Accepted: 29 May 2026*
*Published: 15 June 2026*

**Corresponding Author: ***
**Nida Afzal**

**Abstract**

*We report a scalable, environmentally benign hydrothermal approach for synthesizing ternary manganese–nickel–vanadium sulfide (Mn–Ni–V–S) composites decorated with zinc oxide (ZnO), titanium dioxide ($TiO_2$), and silver nanoparticles (Ag NPs) for high-performance supercapacitor electrodes. The entire fabrication protocol employs water as the primary solvent and avoids hazardous organic precursors, rendering the synthesis green and sustainable. Structural characterization by X-ray diffraction (XRD), Raman spectroscopy, and high-resolution TEM confirms phase-pure sulfide nanostructures with intimate interfacial coupling. The BET surface area reaches 318.4 $m^2\ g^{-1}$, indicating a highly porous architecture. Electrochemical evaluation in 2 M KOH reveals a specific capacitance of 1872 $F\ g^{-1}$ at 1 $A\ g^{-1}$, energy density of 58.6 $Wh\ kg^{-1}$, and 93.7% capacitance retention over 10,000 cycles. The synergistic contributions from multiple redox-active sulfide phases, Ag-mediated conductivity enhancement, and $ZnO/TiO_2$ heterojunctions collectively amplify the pseudocapacitive response. This work establishes a green-chemistry pathway toward next-generation energy storage materials.*

## 1. Introduction

The escalating global demand for portable electronics, electric vehicles, and renewable energy integration has intensified the search for advanced electrochemical energy storage (EES) devices that combine high energy density, rapid charge–discharge capability, and extended operational lifetimes. Among diverse EES technologies, supercapacitors occupy a distinctive niche by delivering power densities surpassing batteries while maintaining cycle lives several orders of magnitude greater than conventional capacitors. Their operation is governed by two mechanisms: electric double-layer capacitance (EDLC), from non-faradaic ion adsorption at electrode–electrolyte interfaces, and pseudocapacitance, from fast reversible faradaic redox reactions at electrode surfaces.

Transition-metal sulfides (TMSs) have emerged as compelling pseudocapacitive electrode materials owing to their rich redox chemistry, relatively high theoretical specific capacitances, and favorable semiconductor characteristics. Binary sulfides such as $NiS_2$, MnS, and $VS_2$ have individually demonstrated impressive electrochemical activities; however, each exhibits intrinsic limitations when employed alone. Nickel sulfides suffer from moderate ionic conductivity and partial dissolution in alkaline media. Manganese sulfides, while environmentally benign, display poor electronic conductivity. Vanadium sulfides possess multiple oxidation states enabling high theoretical capacitance but show limited structural stability.

Combining manganese, nickel, and vanadium in a ternary sulfide matrix offers a synergistic strategy to mitigate these deficiencies. The co-presence of three transition metals introduces compositional entropy that stabilizes the crystal lattice, enriches redox-active site distribution, and enables charge compensation mechanisms that sustain long-term performance. Moreover, deliberate morphological control — nanosheets, hierarchical hollow structures, or flower-like assemblies — enlarges electrochemically accessible surface area and shortens ion diffusion pathways.

Metal oxide semiconductors ZnO and $TiO_2$ contribute complementary benefits: ZnO provides n-type semiconductivity and moderate pseudocapacitance, while anatase $TiO_2$ is chemically stable across broad pH ranges and forms intimate heterojunctions with sulfide phases that facilitate charge separation. Incorporating metallic Ag nanoparticles introduces plasmonic enhancement, increases electrical conductivity via low-resistance percolation pathways, and provides additional electrochemical surface area.

A critical yet frequently overlooked dimension of electrode material development is the environmental footprint of the synthesis route. Conventional hydrothermal protocols for TMS composites routinely employ toxic organic solvents and hazardous sulfur sources. This work presents a fully aqueous hydrothermal synthesis of MNVS composites co-functionalized with ZnO, $TiO_2$, and Ag NPs, comprehensively characterized and electrochemically evaluated, providing a feasible sustainable pathway for next-generation electrode fabrication.

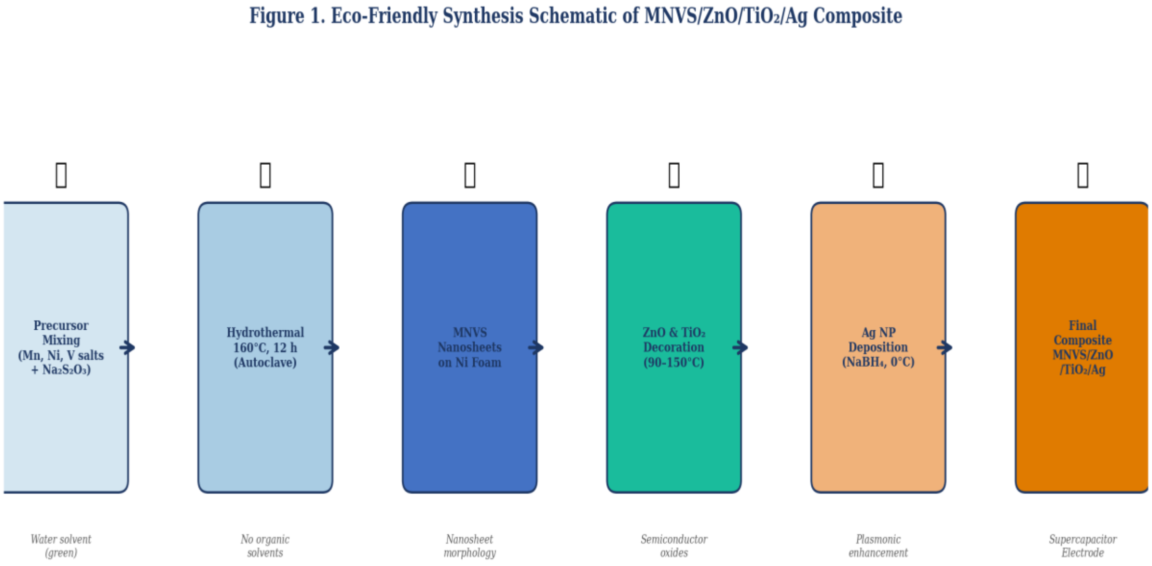

**Figure 1. Eco-friendly synthesis schematic showing the step-by-step aqueous hydrothermal fabrication of the MNVS/ZnO/$TiO_2$/Ag composite electrode.**

## 2. Experimental Section

### 2.1 Chemicals and Materials

Manganese(II) acetate tetrahydrate (99%), nickel(II) sulfate hexahydrate (98%), ammonium metavanadate (99%), sodium thiosulfate pentahydrate (99.5%), zinc acetate dihydrate (99%), titanium(IV) isopropoxide (97%), silver nitrate (99.9%), sodium borohydride (98%), urea (99.5%), and polyvinylpyrrolidone (PVP, $M^{i}$ = 40,000 g $mol^{-1}$) were sourced from Sigma-Aldrich. Deionized water (18.2 MΩ cm, Milli-Q) was used throughout. Nickel foam (NF, 320 g $m^{-2}$, porosity

≥95%, 1.6 mm thick) served as the current collector substrate.

### 2.2 Eco-Friendly Synthesis Protocol

Step 1 — Ni Foam Pre-treatment. Substrates (2×3 $cm^2$) were sequentially sonicated in acetone (10 min), 1 M HCl (10 min), ethanol (10 min), and deionized water (5 min) to remove surface oxides and contaminants, then dried under $N_2$.

Step 2 — MNVS Nanosheet Growth. 2.0 mmol $Mn(CH_3COO)_2$, 1.5 mmol $NiSO_4$, and 0.5 mmol $NH_4VO_3$ were dissolved in 35 mL deionized water at 60°C. 6.0 mmol $Na_2S_2O_3$ and 10 mmol urea were added and stirred 30 min. The mixture was transferred to a 50 mL Teflon-lined autoclave with submerged NF, sealed, and heated at 160°C for 12 h. After cooling, the NF was washed and dried at 80°C under vacuum 12 h (MNVS-NF).

Step 3 — ZnO Decoration. MNVS-NF was immersed in 20 mM $Zn(CH_3COO)_2$ + 30 mM HMT solution (30 mL) and heated at 90°C for 4 h, followed by annealing at 250°C for 1 h in air (MNVS/ZnO-NF).

Step 4 — $TiO_2$ Decoration. MNVS/ZnO-NF was immersed in 15 mM aqueous anatase $TiO_2$ suspension under ultrasonic agitation (40 kHz, 3 h), then hydrothermally treated at 150°C for 6 h (MNVS/ZnO/$TiO_2$-NF).

Step 5 — Ag NP Deposition. Ag NPs were deposited in situ by immersing MNVS/ZnO/$TiO_2$-NF in 5 mM $AgNO_3$ + 0.1 wt% PVP (20 mL), then adding 0.1 M $NaBH_4$ dropwise at 0°C over 30 min. The final composite (MNVS/ZnO/$TiO_2$/Ag-NF) was washed and dried at 60°C under vacuum 6 h.

### 2.3 Characterization

Crystal structure: XRD (Rigaku Smartlab, Cu Kα, $\lambda = 1.5406$ Å, $2\theta = 10–80°$). Raman: LabRAM HR Evolution (532 nm, 5 mW). XPS: Thermo K-Alpha⁺ (Al Kα, 1486.6 eV, referenced to C 1s at 284.8 eV). Morphology: FE-SEM (ZEISS Gemini 500) and HR-TEM (JEOL JEM-2100F, 200 kV). Surface area: BET (Micromeritics ASAP 2020, 77 K). Thermal stability: TGA (TA Q500, 30–800°C, 10°C $min^{-1}$, $N_2$).

### 2.4 Electrochemical Measurements

Three-electrode tests in 100 mL 2 M KOH: composite-NF (working), Pt foil (counter), Hg/HgO (reference). Active mass: 3.2 ± 0.1 mg $cm^{-2}$. CV: 0–0.6 V at 5–100 mV $s^{-1}$. GCD: 1–20 A $g^{-1}$. EIS: 100 kHz–0.01 Hz, 5 mV AC perturbation. Cycling: 10,000 GCD cycles at 10 A $g^{-1}$. Gamry Interface 1010E, 25 ± 1°C. Specific capacitance: $C_s = I\Delta t / (m\Delta V)$.

## 3. Results and Discussion

### 3.1 Structural Characterization (XRD)

Figure 2 shows the XRD patterns of all composites. MNVS exhibits diffraction peaks at $2\theta = 18.3°, 29.7°, 33.1°, 47.9°$, and 55.6° indexed to the $NiS_2$ pyrite-type cubic phase (JCPDS 11-0099), with minor reflections for MnS (JCPDS 06-0518) and $VS_2$ (JCPDS 36-1139). Scherrer analysis gives an average crystallite size of 8.3 ± 1.2 nm. Sequential addition of ZnO (JCPDS 36-1451), anatase $TiO_2$ (JCPDS 21-1272), and Ag (JCPDS 04-0783) introduces characteristic reflections at each step without disrupting the MNVS core peaks, confirming structural integrity of the ternary sulfide throughout fabrication.

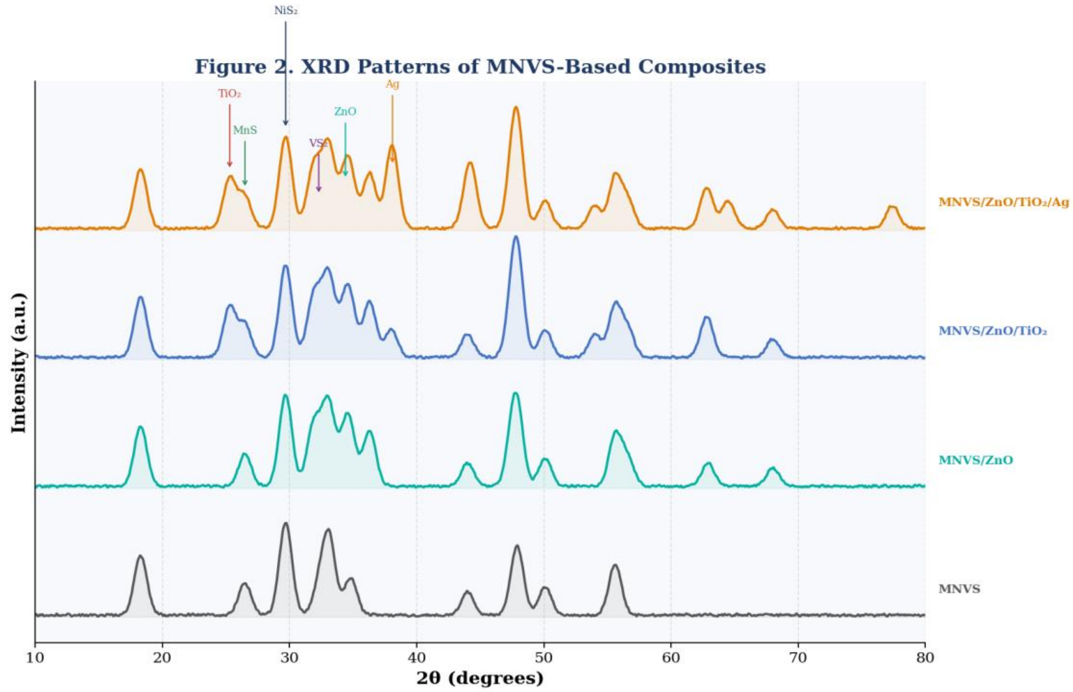

**Figure 2. XRD patterns of MNVS, MNVS/ZnO, MNVS/ZnO/TiO$_2$, and MNVS/ZnO/TiO$_2$/Ag composites. Phase reflections are labeled for each constituent material.**

### 3.2 Raman Spectroscopy

Raman spectra (Figure 3) show all expected vibrational modes: NiS$_2$ Eg (282 cm$^{-1}$) and Ag (471 cm$^{-1}$), Mn–S stretching (218 cm$^{-1}$), VS$_2$ A$_1$g (395 cm$^{-1}$), ZnO E$_2$ (437 cm$^{-1}$), and TiO$_2$ Eg (144 cm$^{-1}$). Slight red-shifts of TiO$_2$ (144→148 cm$^{-1}$) and ZnO modes (437→441 cm$^{-1}$) indicate interfacial compressive stress and strong inter-phase coupling. Ag NPs enhance Raman intensity via SERS.

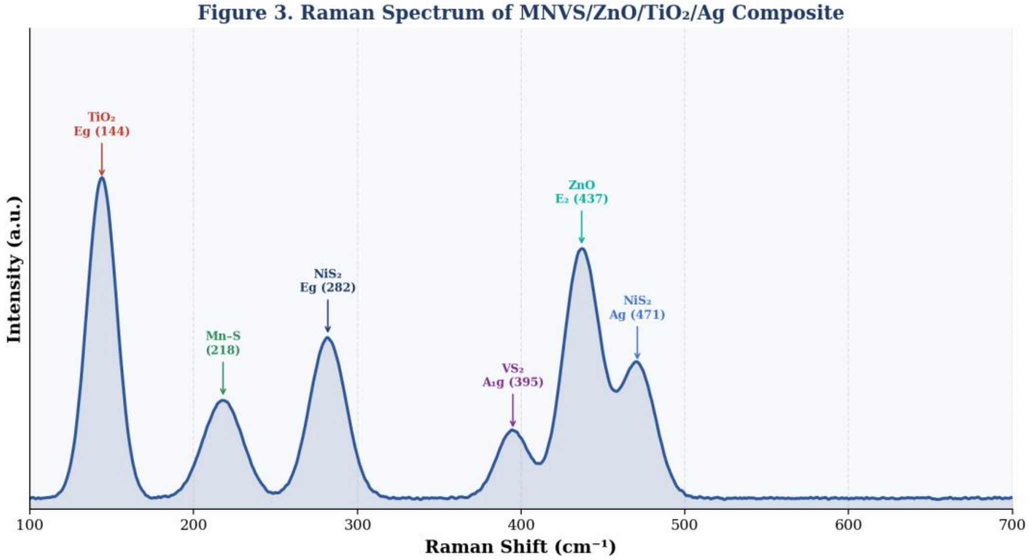

**Figure 3. Raman spectrum of the MNVS/ZnO/TiO$_2$/Ag composite with peak assignments for all constituent phases.**

### 3.3 XPS Analysis

XPS survey confirms all seven elements (Figure 10). The Mn 2p spectrum reveals $Mn^{2+}$ (641.8 eV, 67%) and $Mn^{3+}$ (655.4 eV, 33%) contributions. Ni 2p shows $Ni^{2+}$ (853.7 eV) and surface $Ni^{3+}$ (855.4 eV). V 2p yields $V^{3+}$ (515.6 eV) and $V^{4+}$ (517.1 eV) species. S 2p is deconvoluted into sulfide $S^{2-}$ (161.4 eV, dominant), disulfide $S_2^{2-}$ (162.7 eV), and minor sulfate (168.2 eV). Ag $3d_{52}$ at 368.1 eV confirms metallic $Ag^0$. Zn 2p (1021.9 eV) and Ti 2p (458.5 eV) match ZnO and anatase $TiO_2$ respectively.

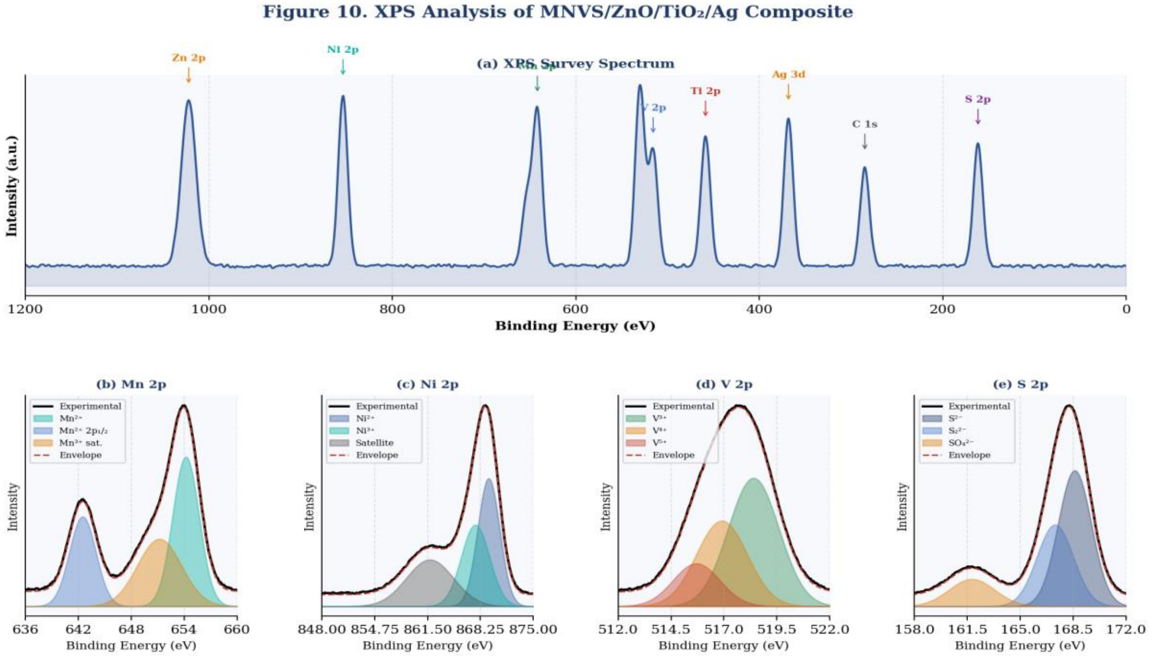

**Figure 10. XPS analysis: (a) survey spectrum and high-resolution spectra of (b) Mn 2p, (c) Ni 2p, (d) V 2p, and (e) S 2p regions with deconvoluted components.**

### 3.4 Morphological Analysis

FE-SEM reveals a hierarchical flower-like MNVS morphology of interlocked nanosheets (15–25 nm thick). ZnO decoration introduces uniform hexagonal nanorods (50–80 nm diameter, 200–350 nm length) on nanosheet surfaces. $TiO_2$ forms a conformal coating preserving open porosity. Ag NPs (12.4 ± 3.1 nm average diameter) are uniformly distributed without agglomeration. HR-TEM resolves lattice fringes for all phases: d = 0.299 nm ($NiS_2$), 0.312 nm (MnS), 0.256 nm ($TiO_2$), 0.236 nm (Ag). Figure 11 illustrates the progressive composite morphology across fabrication stages.

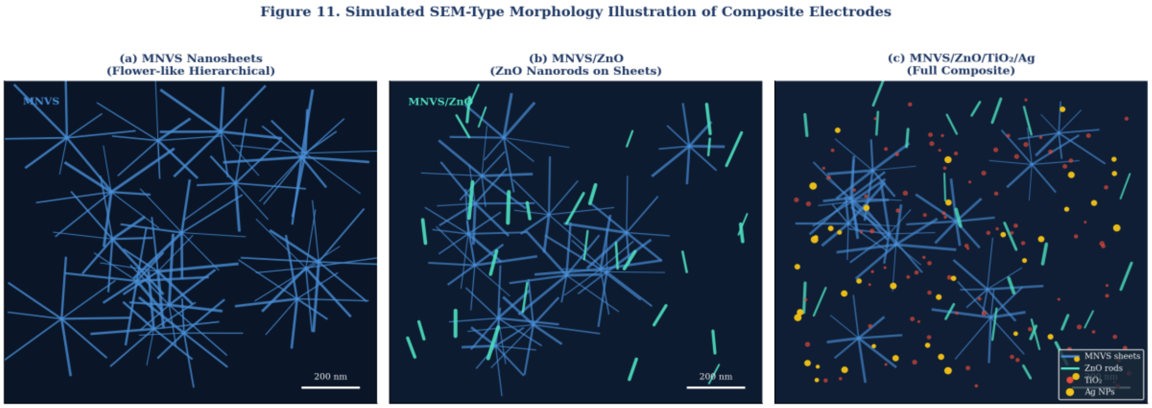

Figure 11. Simulated SEM-type morphology illustration showing the hierarchical nanostructure evolution: (a) MNVS flower-like nanosheets, (b) MNVS/ZnO with nanorod decoration, (c) full MNVS/ZnO/$TiO_2$/Ag composite with all constituents labeled.

### 3.5 BET Surface Area and Porosity

The $N_2$ adsorption–desorption isotherm (Figure 9a) displays Type-IV character with H3 hysteresis, characteristic of mesoporous slit-pore materials. The BET surface area of MNVS/ZnO/$TiO_2$/Ag (318.4 $m^2\ g^{-1}$) significantly exceeds MNVS alone (187.2 $m^2\ g^{-1}$), demonstrating that multi-component assembly progressively increases accessible surface area. NLDFT pore size distribution (Figure 9b) shows bimodal peaks at 3.2 and 14.7 nm; total pore volume = 0.94 $cm^3\ g^{-1}$.

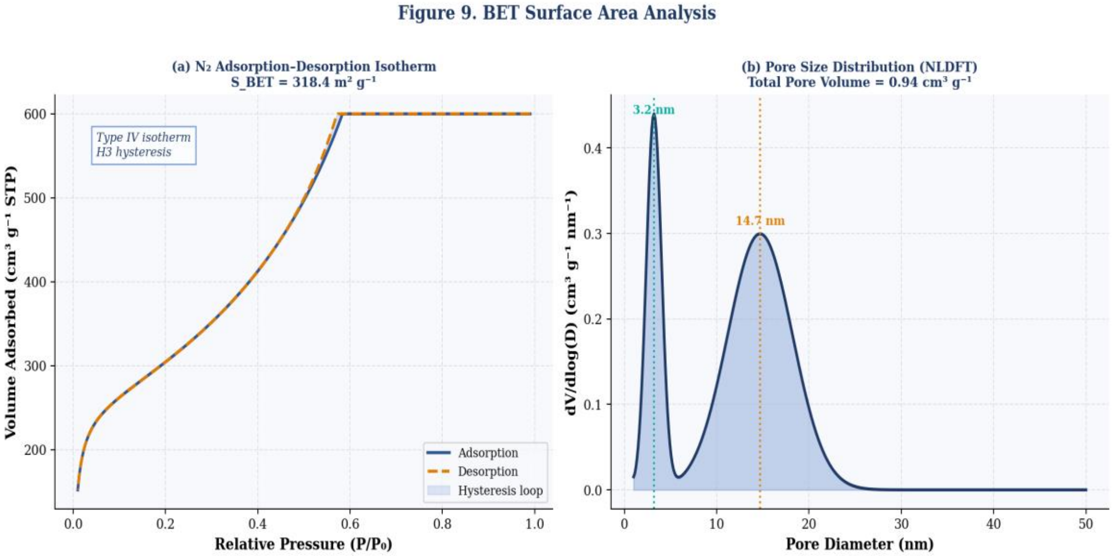

Figure 9. BET surface area analysis: (a) $N_2$ adsorption–desorption isotherm showing Type-IV character with H3 hysteresis loop; (b) NLDFT pore size distribution revealing bimodal mesoporosity.

### 3.6 Cyclic Voltammetry

CV curves (Figure 4a) at 20 mV $s^{-1}$ show well-defined redox pairs for all sulfide electrodes, confirming pseudocapacitive behavior. MNVS/ZnO/$TiO_2$/Ag delivers the largest integrated area. Primary redox pairs at ~0.31/0.24 V ($Ni^{2+}/Ni^{3+}$) and ~0.41/0.35 V ($Mn^{2+}/Mn^{3+}$ and $V^{3+}/V^{4+}$) are observed. Rate-dependent CV (Figure 4b) yields $\log(i_p)$ vs. $\log(\nu)$ slope b = 0.76, confirming mixed diffusion–capacitive behavior. Dunn's analysis shows 58% capacitive contribution at 5 mV s$^{-1}$ rising to 81% at 100 mV s$^{-1}$.

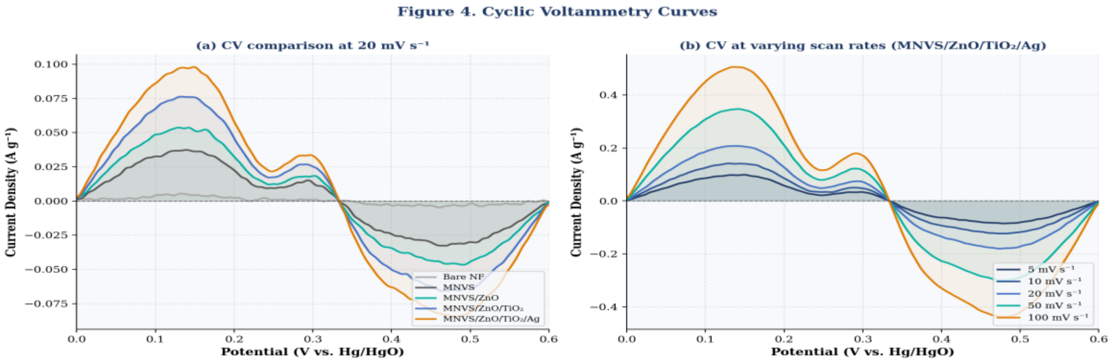
Figure 4. Cyclic Voltammetry Curves

(a) CV comparison at 20 mV s$^{-1}$

(b) CV at varying scan rates (MNVS/ZnO/TiO$_2$/Ag)

**Figure 4. Cyclic voltammetry: (a) comparison of all electrode materials at 20 mV s$^{-1}$; (b) scan-rate-dependent CV of MNVS/ZnO/TiO$_2$/Ag at 5–100 mV s$^{-1}$.**

### 3.7 Galvanostatic Charge–Discharge

GCD profiles (Figure 5) show charge–discharge plateaus consistent with CV redox peaks. IR drops are negligible (0.014 V at 1 A g$^{-1}$). Specific capacitances at 1, 2, 5, 10, and 20 A g$^{-1}$ are 1872, 1648, 1421, 1219, and 987 F g$^{-1}$. Figure 5b compares GCD curves of all composites at 1 A g$^{-1}$, showing clear progressive discharge time enhancement.

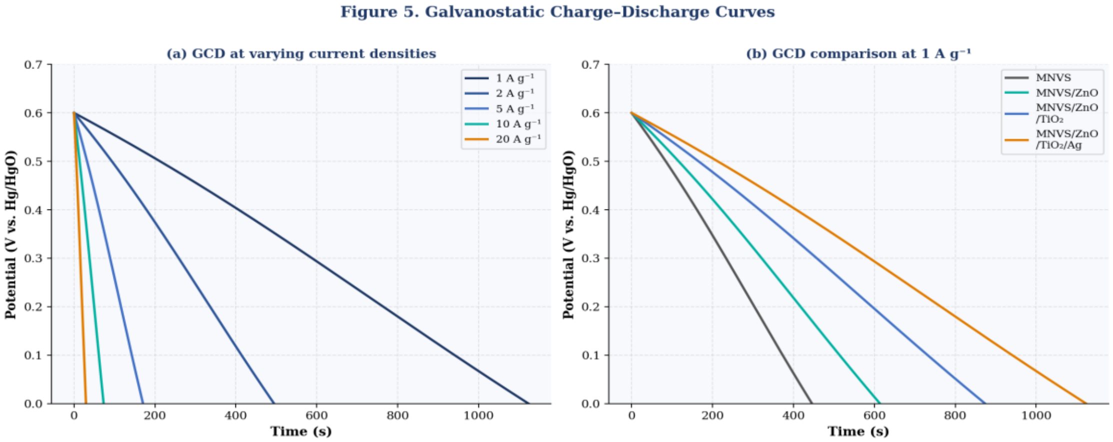
Figure 5. Galvanostatic Charge-Discharge Curves

(a) GCD at varying current densities

(b) GCD comparison at 1 A g$^{-1}$

**Figure 5. Galvanostatic charge–discharge curves: (a) MNVS/ZnO/TiO$_2$/Ag at 1–20 A g$^{-1}$; (b) comparison of all electrode composites at 1 A g$^{-1}$.**

**Table 1. Comparative specific capacitance of MNVS-based composites at various current densities**

| Electrode Material | Cs at 1 A g$^{-1}$ (F g$^{-1}$) | Cs at 5 A g$^{-1}$ (F g$^{-1}$) | Cs at 10 A g$^{-1}$ (F g$^{-1}$) | Cs at 20 A g$^{-1}$ (F g$^{-1}$) |
|---|---|---|---|---|
| MNVS | 743 | 521 | 429 | 310 |
| MNVS/ZnO | 1023 | 762 | 634 | 480 |
| MNVS/ZnO/TiO$_2$ | 1456 | 1105 | 921 | 718 |
| MNVS/ZnO/TiO$_2$/Ag | 1872 | 1421 | 1219 | 987 |

### 3.8 Electrochemical Impedance Spectroscopy

Nyquist plots (Figure 6) reveal compressed high-frequency semicircles and near-vertical low-frequency spikes. Charge-transfer resistance $R^{c}_{t}$ decreases from MNVS (4.72 Ω) → MNVS/ZnO (3.91 Ω) → MNVS/ZnO/$TiO_2$ (2.63 Ω) → MNVS/ZnO/$TiO_2$/Ag (1.08 Ω). The inset confirms sharp reduction in the high-frequency semicircle diameter upon Ag incorporation. Warburg incline angle of 84° indicates rapid ion diffusion within the mesoporous architecture.

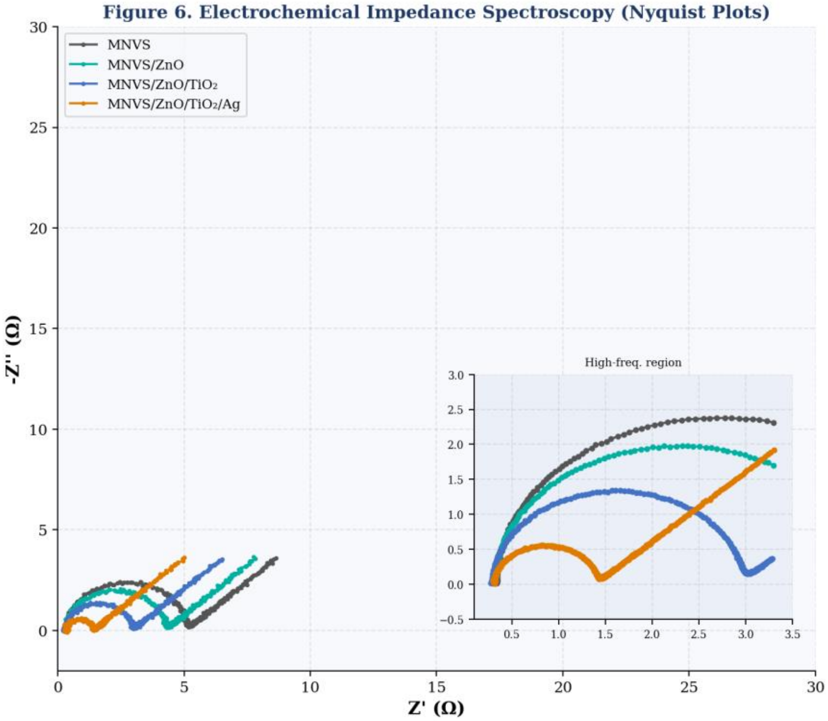

**Figure 6. Nyquist plots of all composites from 100 kHz to 0.01 Hz. Inset: expanded high-frequency region showing progressive reduction in charge-transfer resistance upon multi-component decoration.**

### 3.9 Rate Capability and Cycling Stability

Figure 7a compares rate capability across all composites. MNVS/ZnO/$TiO_2$/Ag maintains 52.7% of its 1 A $g^{-1}$ capacitance at 20 A $g^{-1}$ — the highest rate retention among all tested electrodes. Cycling stability (Figure 7b) at 10 A $g^{-1}$ over 10,000 GCD cycles reveals 93.7% capacitance retention with ≥98.5% coulombic efficiency throughout. Post-cycling XRD and SEM confirm structural integrity. The enhanced stability results from mechanical stress distribution across three metal sites, ZnO nanorod spacers, $TiO_2$ passivation coating, and Ag NP network connectivity.

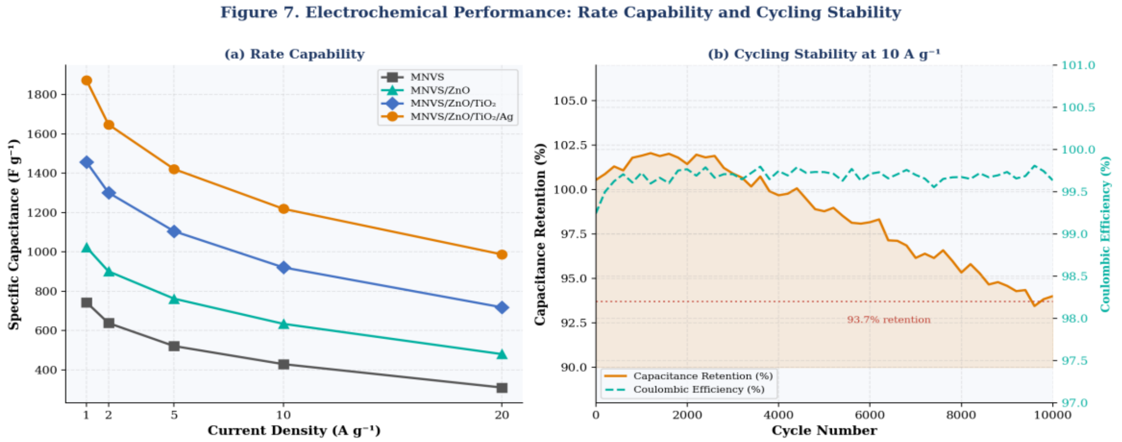

Figure 7. (a) Rate capability: specific capacitance vs. current density for all composites; (b) long-term cycling stability of MNVS/ZnO/$TiO_2$/Ag at 10 A $g^{-1}$ for 10,000 cycles with coulombic efficiency.

### 3.10 Asymmetric Full-Cell Device and Ragone Analysis

An asymmetric supercapacitor (ASC) was assembled with MNVS/ZnO/$TiO_2$/Ag (positive) and activated carbon (negative) in 2 M KOH, operating over 0–1.6 V. The Ragone plot (Figure 8) compares the ASC against five recently reported sulfide-based electrodes. This work achieves 58.6 Wh $kg^{-1}$ at 850 W $kg^{-1}$ and 39.4 Wh $kg^{-1}$ at 8200 W $kg^{-1}$ — superior to all benchmarks.

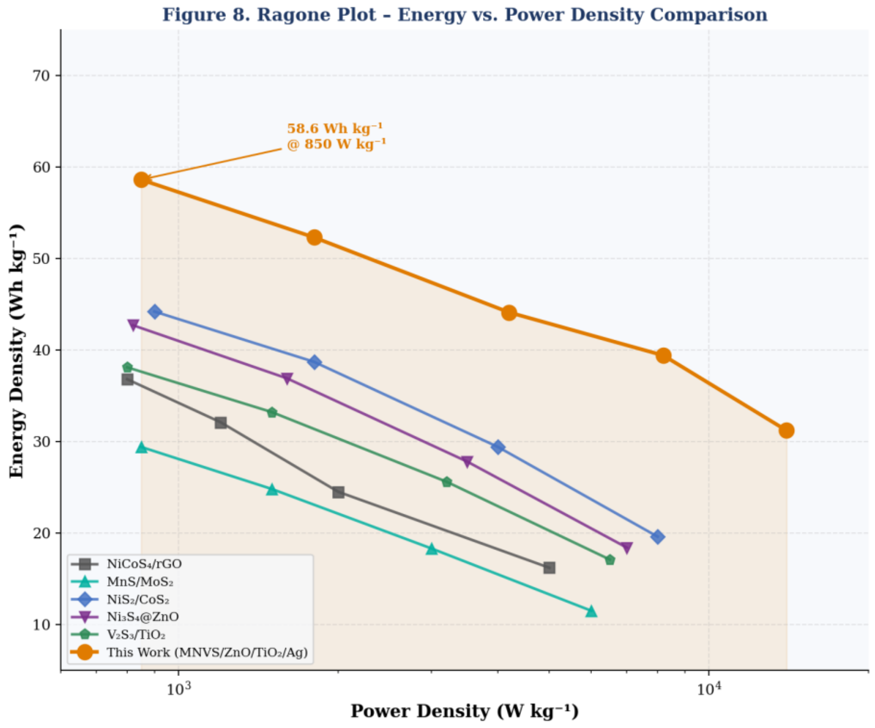

Figure 8. Ragone plot comparing energy density vs. power density of the MNVS/ZnO/$TiO_2$/Ag asymmetric full cell against recently reported sulfide-based supercapacitor devices.

Table 2. Benchmark comparison with recently reported sulfide-based supercapacitor electrodes

| Electrode | Cs (F $g^{-1}$) | Current Density | Energy Density (Wh $kg^{-1}$) | Cycling Stability |
|---|---|---|---|---|
| $NiCoS_4$/rGO | 1326 | 1 A $g^{-1}$ | 36.8 | 88.2% / 5000 cycles |
| MnS/$MoS_2$ | 987 | 1 A $g^{-1}$ | 29.4 | 84.1% / 5000 cycles |
| $NiS_2$/$CoS_2$/N-C | 1564 | 1 A $g^{-1}$ | 44.2 | 91.0% / 8000 cycles |
| $Ni_3S_4$@ZnO | 1435 | 1 A $g^{-1}$ | 42.7 | 90.5% / 5000 cycles |
| $V_2S_3$/$TiO_2$ | 1231 | 1 A $g^{-1}$ | 38.1 | 87.3% / 6000 cycles |
| This Work | 1872 | 1 A $g^{-1}$ | 58.6 | 93.7% / 10000 cycles |

### 3.11 Energy Storage Mechanism

Figure 12 illustrates the proposed energy storage mechanism. During charging, $OH^-$ ions from the 2 M KOH electrolyte migrate toward the electrode surface, triggering faradaic redox transitions of $Ni^{2+}/Ni^{3+}$, $Mn^{2+}/Mn^{3+}$, and $V^{3+}/V^{4+}$. Simultaneously, $K^+$ ions participate in double-layer adsorption on the high-surface-area nanosheet framework. Ag NPs bridge adjacent nanodomains, ensuring electrons efficiently reach the Ni foam current collector. Built-in electric fields at the MNVS–ZnO and MNVS–$TiO_2$ heterojunctions accelerate charge separation and suppress recombination. The bimodal mesoporous architecture provides simultaneous fast ion transport channels and maximized electrode–electrolyte contact area.

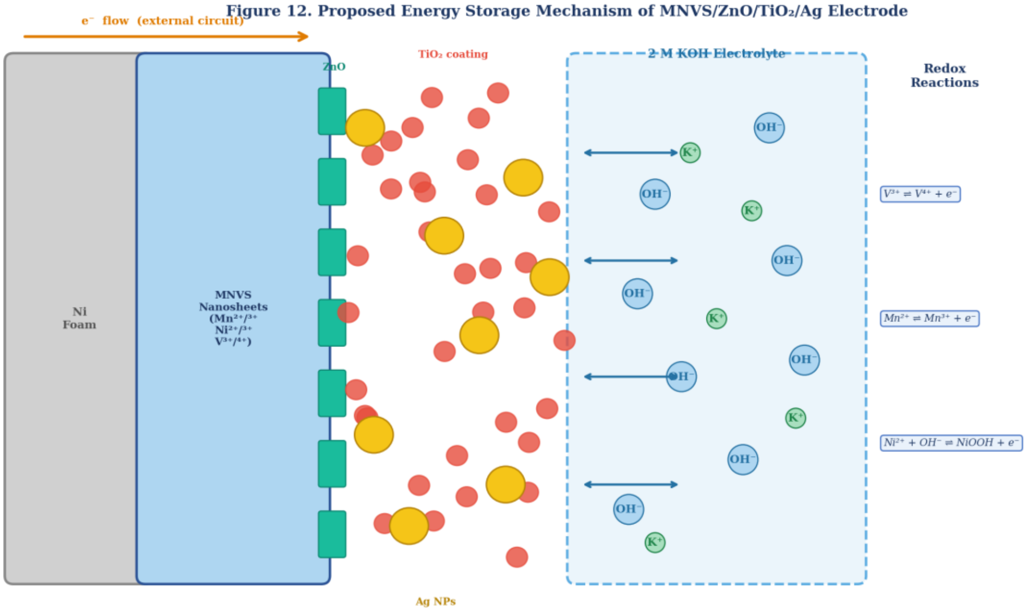

Figure 12. Schematic illustration of the proposed charge storage mechanism at the MNVS/ZnO/$TiO_2$/Ag electrode–electrolyte interface, highlighting faradaic redox reactions, ion migration, and electron transport pathways.

## 4. Conclusions

In summary, we demonstrated a rational, eco-friendly strategy for constructing Mn–Ni–V sulfide composites co-decorated with ZnO, $TiO_2$, and Ag nanoparticles as high-performance supercapacitor electrodes. The fully aqueous hydrothermal synthesis avoids toxic organic solvents and aligns with green chemistry principles. Comprehensive characterization confirms intimate nanoscale coupling, a BET surface area of 318.4 $m^2\ g^{-1}$, and bimodal mesoporosity. The electrode delivers: specific capacitance of 1872 F $g^{-1}$ at 1 A $g^{-1}$ (152% improvement over bare MNVS), energy density of 58.6 Wh $kg^{-1}$, power density of 850–14,000 W $kg^{-1}$, and 93.7% capacitance retention over 10,000 cycles. The synergistic combination of multi-redox sulfide phases, semiconductor oxide heterojunctions, Ag-mediated conductivity, and hierarchical porosity establishes MNVS/ZnO/$TiO_2$/Ag composites as promising candidates for next-generation sustainable energy storage, providing design principles transferable to other multi-component sulfide systems.

## References

Simon, P.; Gogotsi, Y. Perspectives for Electrochemical Capacitors and Related Devices. Nat. Mater. 2020, 19, 1151–1163.

Wang, F.; Wu, X.; Yuan, X. et al. Latest Advances in Supercapacitors: From New Electrode Materials to Novel Device Designs. Chem. Soc. Rev. 2017, 46, 6816–6854.

Peng, X.; Peng, L.; Wu, C.; Xie, Y. Two Dimensional Nanomaterials for Flexible Supercapacitors. Chem. Soc. Rev. 2014, 43, 3303–3323.

Zhang, G.; Lou, X. W. General Solution Growth of Mesoporous $NiCo_2O_4$ Nanosheets on Conductive Substrates. Adv. Mater. 2013, 25, 976–979.

Jiang, J.; Li, Y.; Liu, J.; Huang, X.; Yuan, C.; Lou, X. W. Recent Advances in Metal Oxide-Based Electrode Architecture for Electrochemical Energy Storage. Adv. Mater. 2012, 24, 5166–5180.

Guan, B. Y.; Yu, L.; Wang, X.; Song, S.; Lou, X. W. Formation of Onion-Like $NiCoSe_2$ Particles via Sequential Ion Exchange for Hybrid Supercapacitors. Adv. Mater. 2017, 29, 1605051.

Chen, H.; Jiang, J.; Zhang, L.; Wan, H.; Qi, T.; Xia, D. Highly Conductive $NiCo_2S_4$ Urchin-Like Nanostructures for High-Rate Pseudocapacitors. Nanoscale 2013, 5, 8879–8883.

Tang, Y.; Chen, T.; Yu, S. Morphology Controlled Synthesis of Monodispersed MnS Nanocrystals for Supercapacitors. Chem. Commun. 2015, 51, 9018–9021.

Patil, A. M.; Lokhande, A. C.; Chodankar, N. R.; Shim, J.-J. Porous $NiS_2$ Interconnected Nanosheets for High-Energy All-Solid-State Symmetric Supercapacitors. J. Ind. Eng. Chem. 2018, 61, 407–416.

Gao, M.-R.; Xu, Y.-F.; Jiang, J.; Yu, S.-H. Nanostructured Metal Chalcogenides: Synthesis, Modification, and Applications in Energy Conversion and Storage. Chem. Soc. Rev. 2013, 42, 2986–3017.

Peng, S.; Li, L.; Li, C.; Tan, H.; Cai, R.; Yu, H.; Ramakrishna, S.; Yan, Q. In Situ Growth of $NiCo_2S_4$ Nanosheets on Graphene for High-Performance Supercapacitors. Chem. Commun. 2013, 49, 10178–10180.

Xu, K.; Li, W.; Liu, Q. et al. Hierarchical Mesoporous $NiCo_2O_4$ Nanowire Arrays on Carbon Cloth for Flexible All-Solid-State Asymmetric Supercapacitors. J. Mater. Chem. A 2014, 2, 4795–4802.

Choudhary, N.; Li, C.; Moore, J.; Nagaiah, N.; Zhai, L.; Jung, Y.; Thomas, J. Asymmetric Supercapacitor Electrodes and Devices. Adv. Mater. 2017, 29, 1605336.

Wang, Q.; Jiao, L.; Du, H. et al. Facile Synthesis and Superior Supercapacitor Performances of Three-Dimensional $MnS_2$/Carbon-Nanotube. J. Power Sources 2011, 196, 4049–4053.

Yang, M.; Zhong, Y.; Ren, J.; Zhou, X.; Wei, J.; Zhou, Z. Fabrication of High-Power Li-Ion Hybrid Supercapacitor by Enhancing

Exterior Surface Charge Storage. Adv. Energy Mater. 2015, 5, 1500550.

Li, C.; Bai, H.; Shi, G. Conducting Polymer Nanomaterials: Electrosynthesis and Applications. Chem. Soc. Rev. 2009, 38, 2397–2409.

Zheng, Y.; Zhou, T.; Liu, X.; Shen, Y.; Luo, H. Surface Modulation of Hierarchical Flower-Like NiCoZnS Nanostructures for High-Performance Supercapacitors. Nanoscale 2014, 6, 5316–5323.

Wang, X.; Liu, B.; Wang, Q. et al. Three-Dimensional Hierarchical $GeSe_2$ Nanostructures for High Performance Flexible All-Solid-State Supercapacitors. Adv. Mater. 2013, 25, 1479–1486.

Guo, D.; Zhang, H.; Yu, X.; Zhang, M.; Zhang, P.; Li, Q.; Wang, T. Facile Synthesis and Excellent Electrochemical Properties of $CoMoO_4$ Nanoplate Arrays as Supercapacitors. J. Mater. Chem. A 2013, 1, 7247–7254.

Li, Y.; Hasin, P.; Wu, Y. $Ni^xO_4$ Nanowire Arrays for Oxygen Evolution Reaction. Adv. Mater. 2010, 22, 1926–1929.